Received: 12 June 2023 | Accepted: 14 June 2023

DOI: 10.1002/asna.20230103

Astronomische Nachrichten

PROCEEDING

Evaluating the GeoSnap 13-μm cutoff HgCdTe detector for mid-IR ground-based astronomy

Jarron M. Leisenring[1] | Dani Atkinson[2] | Rory Bowens[2] | Vincent Douence[3] | William F. Hoffmann[1] | Michael R. Meyer[2] | John Auyeung[3] | James Beletic[3] | Mario S. Cabrera[4,5] | Alexandra Z. Greenbaum[6] | Philip Hinz[7] | Derek Ives[8] | William J. Forrest[4] | Craig W. McMurtry[4] | Judith L. Pipher[4,†] | Eric Viges[2]

[1]Steward Observatory and Department of Astronomy, University of Arizona, Tucson, Arizona

[2]Department of Astronomy, University of Michigan, Ann Arbor, Michigan

[3]Teledyne Imaging Systems, Camarillo, California

[4]Deptartment of Physics & Astronomy, University of Rochester, Rochester, New York

[5]Conceptual Analytics LLC, Glenn Dale, Maryland

[6]IPAC, CalTech, Pasadena, California

[7]Astronomy & Astrophysics Department, UC Santa Cruz, Santa Cruz, California

[8]EDES-ELE-DoE, ESO, Garching bei München, Germany

Correspondence
Jarron M. Leisenring, Steward Observatory and Department of Astronomy, University of Arizona, 933 N Cherry Ave, Tucson, AZ 85721, USA.
Email: jarronl@arizona.edu

Funding information
Heising-Simons Foundation, Grant/Award Number: 2020-1699; Templeton World Charity Foundation, Grant/Award Number: TWCF0330

Abstract

New mid-infrared HgCdTe (MCT) detector arrays developed in collaboration with Teledyne Imaging Sensors (TIS) have paved the way for improved 10-μm sensors for space- and ground-based observatories. Building on the successful development of longwave HAWAII-2RGs for space missions such as NEO Surveyor, we characterize the first 13-μm GeoSnap detector manufactured to overcome the challenges of high-background rates inherent in ground-based mid-IR astronomy. This test device merges the longwave HgCdTe photosensitive material with Teledyne's 2048×2048 GeoSnap-18 (18-μm pixel) focal plane module, which is equipped with a capacitive transimpedance amplifier (CTIA) readout circuit paired with an onboard 14-bit analog-to-digital converter (ADC). The final assembly yields a mid-IR detector with high QE, fast readout (>85 Hz), large well depth (>1.2 million electrons), and linear readout. Longwave GeoSnap arrays would ideally be deployed on existing ground-based telescopes as well as the next generation of extremely large telescopes. While employing advanced adaptive optics (AO) along with state-of-the-art diffraction suppression techniques, instruments utilizing these detectors could attain background- and diffraction-limited imaging at inner working angles <10 λ/D, providing improved contrast-limited performance compared with JWST MIRI while operating at comparable wavelengths. We describe the performance characteristics of the 13-μm GeoSnap array operating between 38 *and* 45 K, including quantum efficiency, well depth, linearity, gain, dark current, and frequency-dependent ($1/f$) noise profile.

KEYWORDS

detectors, image sensors, infrared arrays, HgCdTe, MCT, CMOS

†Deceased.

This is an open access article under the terms of the Creative Commons Attribution-NonCommercial-NoDerivs License, which permits use and distribution in any medium, provided the original work is properly cited, the use is non-commercial and no modifications or adaptations are made.
© 2023 The Authors. *Astronomische Nachrichten* published by Wiley-VCH GmbH.

1 | INTRODUCTION

Ground-based mid-infrared (mid-IR) instrumentation has the ability to revolutionize a wide range of astronomical research, but presents significant challenges. Emission from 3 to 13 μm can be used to characterize astrophysical objects over a wide range of temperatures (<100 to >1000 Kelvins), penetrate obscuring dust, investigate physical conditions of environments containing molecules bearing key volatile elements of carbon, nitrogen, and oxygen, and even probe galaxy formation and evolution in the early Universe. However, ground-based mid-IR observing has sometimes been compared with observing in the visible during the daytime with a telescope that is on fire, because all terrestrial objects emit significantly at these wavelengths, providing an overwhelming high background. The development of mid-IR photo-conductive detectors began in the 1960s and progressed rapidly. While many pioneering observations were made with ground-based systems, it was clear that mid-IR astronomy in space would have tremendous returns leading to the launch of IRAS in the 1980s (Neugebauer et al. 1984).

For diffraction-limited observations of point sources, the time to complete an observation at a fixed signal-to-noise (SNR) scales as $D_{\rm tel}^{-4}$ when the dominant source of noise is background radiation. This was achievable from the ground on 4-m class telescopes in the 1990s as long as a bright source remained in the field of view throughout the observing sequence to serve as a reference. Lacking such sources, it was difficult to keep the telescope fixed and integrate for long periods on the same field to reveal faint targets. The advent of tip-tilt secondaries and adaptive optics (AO) led to huge improvements (e.g., Beckers 1993; Davies & Kasper 2012). However, detector limitations such as low quantum efficiency, as well as excess low-frequency noise that required modulating the source on the detector at high frequency (chopping), limited what could be done.

The launch of NASA's *Spitzer Space Telescope* in 2003 provided an extremely sensitive and reliable platform for wide-field mid-IR observations, enabling extraordinary progress, albeit with limited spatial resolution. With the more recent launch of the 6.5-m JWST (Gardner et al. 2006), why should we invest now in ground-based mid-IR? JWST MIRI enables a tremendous leap in mid-IR astronomy with a large field of view and extraordinary sensitivity (Rieke et al. 2015; Wright et al. 2015). Yet, due to the mid-frequency errors in the mirror segments and limited stability and metrology, JWST has limited contrast as a function of λ/D, as demonstrated in Carter et al. (2022). Instead, ground-based telescopes equipped with advanced AO will outperform JWST in the contrast limit around bright sources (cf. Beichman et al. 2019; Boccaletti et al. 2015; Danielski et al. 2018; Delacroix et al. 2013; Ren et al. 2023).

There are many scientific areas where a sensitive high-resolution/contrast mid-IR capability can provide fundamental breakthroughs including: (a) exoplanet detection and characterization; (b) star formation and planet-forming disks; (c) circumstellar environments of evolved stars; (d) warm dust emission in local group star clusters; (e) star forming galaxies and active galactic nuclei in the local Universe; and (f) multiwavelength observations of multiple strong gravitational lens sources at high redshift. Ground-based AO assisted mid-IR imaging is extremely complementary to what JWST can provide.

Currently, there are only two mid-IR detectors on large ground-based telescopes equipped with adaptive optics that have recently been in operation. The NEAR experiment on the ESO VLT (Kasper et al. 2017) was funded by Breakthrough Initiatives to search for Earth-like planets around the nearest stars to the Sun, α Cen A and B. The system utilizes a Raytheon AQUARIUS array with modest quantum efficiency ($\sim$ 40%) and excess low-frequency noise (e.g., Hoffmann et al. 2014). Despite these limitations, the NEAR project produced interesting results (Kasper et al. 2019; Pathak et al. 2021; Viswanath et al. 2021; Wagner et al. 2021), but is no longer available. Another system, NOMIC on the LBTI, also utilizes an AQUARIUS array, with the vast majority of its observations obtained with nulling interferometry (e.g., Ertel et al. 2018).

Teledyne Imaging Sensors (TIS) developed a longwave (<15 μm) large-format (2048 × 2048) HgCdTe (MCT) detector for low-background space-based applications with high quantum efficiency (approaching 90%) and low noise (McMurtry et al. 2013). A parallel effort has produced the GeoSnap array, with deep wells and a fast readout integrated circuit (ROIC) potentially suitable for ground-based astronomy. This new ROIC paired with mid-infrared material could revolutionize ground-based, mid-IR astronomy, particularly when coupled with adaptive optics on 6–12-m telescopes. Such systems on 25–39-m class telescopes would be capable of imaging rocky planets around the nearest stars (e.g., Bowens et al. 2021; Hinz et al. 2010). Here we describe efforts to characterize the GeoSnap array for use in ground-based mid-IR instruments. One such instrument is MIRAC-5, currently being refurbished for use on the MMT with the new MAPS AO system (Bowens et al. 2022; Morzinski et al. 2020).

We describe the GeoSnap device in Section 2 and provide an overview of the test facilities in Section 3. The device's measured characteristics are presented in Section 4, while Section 5 separately discusses observed excess noise.

2 | DEVICE DESCRIPTION

The GeoSnap-18 is a large-format (2048 × 2048) detector array with an 18-μm pixel pitch developed by Teledyne Imaging Sensors (TIS) for fast imaging operations. The standard full frame readout maxes out at 86.7 Hz frame rate, but has capabilities for up to 143.2 Hz. The readout integrated circuit (ROIC) utilizes a capacitive transimpedance amplifier (CTIA), which enables large well depths (1.2–2.6 Me^- and higher) relative to the traditional pixel source follower (~100 ke^-) found in the HAWAII-xRG (HxRG) detector series (Beletic et al. 2008; Jerram & Beletic 2019).

GeoSnap incorporates on-chip electronics for clock timing, bias generation, and 14-bit ADC within a single assembly located at the instrument focal plane. All pixels are exposed simultaneously using a global shutter, differing from standard HxRG operations, which utilize a rolling clocking scheme such that consecutive pixels are addressed at slightly different times (e.g., 10-μs increments). The chip incorporates an integrate while read architecture, which minimizes overheads and maximizes exposure time efficiency. GeoSnap's standard full frame readout can operate below 1 Hz and up to 86.7 Hz frame rate, although frame rates of >140 Hz can be achieved at the cost of reduced ADC resolution (13.2 bits). Vertical window mode enables higher frame rates when reading <2048 rows.

This combination of high speed and large well depths makes these arrays suitable for high-background IR environments. Figure 1 shows an image of the GeoSnap focal plane module SN20561, consisting of a 13-μm cutoff HgCdTe die hybridized onto a single 1024 × 1024 quadrant. The HgCdTe material originated from a program led by the University of Rochester to develop longwave HxRG arrays out to 15 μm (e.g., C. W. McMurtry et al. 2016; Dorn et al. 2018; Cabrera et al. 2019; Cabrera et al. 2020).

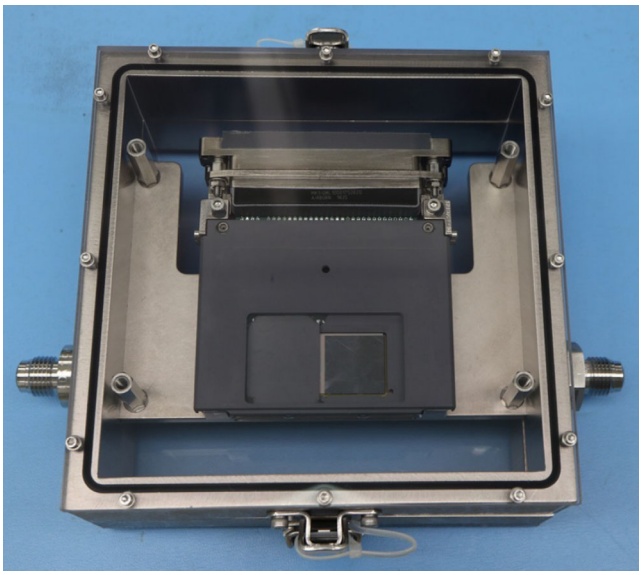


FIGURE 1 The GeoSnap-18 (A0 ROIC) Part Number SN20561 enclosed in its storage case. The hybridized quadrant is evident in the lower right corner, while the three remaining quadrants are covered with a mask. Two layers of ribbon cables connect to the top orientation, carrying power and digital lines.

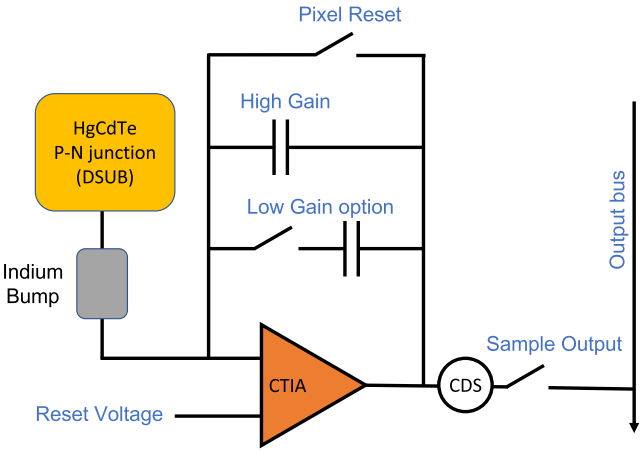


FIGURE 2 Cartoon schematic of CTIA pixel unit cell design.

2.1 | Unit cell

For a typical source follower readout used in the HxRG detectors, photoelectrons travel primarily via diffusion while under the influence of a weak electric field within the photosensitive material (Pain & Fossum 1993; G. Rieke 2002). The output signal is simply a measure of the voltage strength across the HgCdTe p–n junction as photo-generated charge travels across the depletion region. As more electrons are knocked loose, the strength of the electric field drops, which naturally limits well sizes to approximately 100 ke^- depending on the initial configuration of the device's backbias.

For a CTIA circuit as depicted in Figure 2, the input gate of the HgCdTe material is constantly held at the reset voltage during detector operations. The signal is then allowed to accumulate on a capacitor embedded within each pixel unit cell. This readout scheme enables large well depths defined by the capacitors with highly linear outputs.

The GeoSnap multiplexer includes two different gain modes using independent capacitors with different inherent charge-well sizes. Well sizes vary depending on ROIC revision; the A0 version provided for this study was manufactured for nominal well depths of 1.2 Me^- and 90 ke^- for

the low and high gain modes, respectively. The more recent A1 and B0 ROICs have approximately twice the well depths for both gain modes (2.7 Me^- and 190 ke^- for the low and high gain modes, respectively). Read noise in the low gain mode typically runs 5–7 times higher that of high gain (i.e., 150 e^- vs. 25 e^-).

Within an observed frame time, GeoSnap's CTIA circuit performs a number of operations prior to digitization of the signal, including a pixel reset, on-chip CDS, and integration. At the beginning of a frame, the programmable reset duration holds the pixel reset switch closed, preventing signal accumulation on the capacitors. The reset time is configured as a fraction of the total frame time, and integration is simply the remaining frame time minus small internal switching overheads. Prior to integration, the circuit quickly samples and stores the reset state to perform an analog on-chip CDS subtraction of the measured signal. More complex readout modes have been developed to disable the reset and CDS operations within a subsequent number of frames in order to perform a sample-up-the-ramp integration with multiple frames.

The CTIA circuit can also eliminate some problematic detector characteristics that plague observations with HxRG detectors. Since the depletion region of the pixel P–N junction is held constant throughout GeoSnap operations, charge traps remain unfilled since no de-biasing occurs. This effectively removes charge persistence effects and related latent images. In addition, holding all pixel gates at the same constant reset voltage eliminates interpixel capacitance (IPC) caused by capacitive coupling of neighboring pixels (Moore et al. 2004). The constant voltage fields also prevent the "brighter-fatter" phenomenon where a PSF appears to increase in size with brightness due to charge migration from bright pixels to their neighbors during an exposure (Plazas et al. 2018).

Power dissipation at the focal plane is extremely high due to the CTIA circuit being held at a constant reset voltage along with the high-speed readout and onboard digitization. The resulting heat leads to significant ROIC glow that is easily detectable by longwave devices. However, for ground-based mid-IR observations, the background rates from the sky and warm telescope optics dominate over the GeoSnap's self-emission.

2.2 | Readout architecture

The readout electronics used in this study consist of three primary components: the cryogenic focal plane module (FPM), external focal plane electronics (FPE), and processing electronics (PE) board. These are connected in series with various cable harnesses to facilitate communication interfaces and science data transfer. Each of the component contains test pattern modes to generate predictable images to check the electronics' functionality and verify connectivity.

The FPM is comprised of the ROIC, an on-chip 14-bit ADC, bias generation, and a programmable serial interface. Digitized pixel data are converted to 16-bit information and sent through 8 digital output ports mapped to 512×1024 sections of pixels. The image output is passed to the FPE through two ribbon cable harnesses at 1.6 Gbps per output, for a total bandwidth of 12.8 Gbps. In addition to receiving and processing the science pixel data, the FPE provides the power, control, and clock signals to operate the ROIC.

The PE sits between the FPE and host computer, primarily acting as a control interface to the FPE and ROIC as well as converting image data to the Camera Link interface format for ingestion by the host computer. User commands are sent over a USB cable using a standard serial connection. Video data are received by the host computer over four Camera Link cables, each one dedicated to an independent detector quadrant. Data are received by a Matrox Radient ev-CL PCIe frame grabber capable of handling the full 2048×2048 16-bit data at >85 Hz without overheads. We have implemented a Linux driver to continuously process and write contiguous frames in real time.

2.3 | Low operating temperatures

At operating temperatures below 55K, the master voltage reference of the early generation A0 and A1 ROICs is unable to attain its nominal value of 3.0 V, and instead rails at 3.3 V no matter the register setting of the programmable DAC. This is because these ROICs were designed for nominal operations of >77 K. At lower temperatures, the built-in bandgap reference that defines the settable DAC range of the master voltage would substantially increase. The more recent B0 ROIC revision includes an option to use non-bandgap-derived master reference for this range of temperatures.

While all data presented in this work were acquired using an A0 ROIC operating between 35 and 50 K to reduce dark current, preliminary results did not show any deleterious effects to the data when compared with observations acquired at T = 80 K. We conclude that a master reference value of 3.3 V is acceptable for our purposes.

3 | TEST ENVIRONMENTS

The GeoSnap-18 hardware (part SN20561) was first delivered to the University of Arizona in March, 2019 for initial check-out and characterization. Primary test data

were acquired between August and November of 2019 in a refurbished version of the Mid-InfraRed Array Camera (MIRAC) instrument at Arizona (Hoffmann et al. 1993; Hoffmann et al. 1998). The detector and readout electronics were subsequently shipped to the University of Michigan for further testing under dark conditions in the MITTEN cryostat (Bowens et al. 2020).

3.1 | MIRAC testing at AZ

The fifth iteration of the instrument, MIRAC-5's optical design, consists of an off-axis ellipsoid to reimage an intermediate focal plane (located near the instrument entrance window) onto the detector surface housed within a cryogenic environment (Bowens et al. 2022). The entrance aperture wheel has five positions containing three slits ranging from 0.4 to 0.8 mm wide, a pinhole 0.5 mm in diameter, and a large square aperture. A cold pupil stop is positioned after the reimaging optics. Two filter wheels sit immediately after the pupil stop holding over a dozen narrow, medium, and broadband filters throughout the JHKLMN infrared bands as well as blanks to acquire unilluminated observations.

MIRAC is cooled by a Cryomech Pulse Tube cryocooler, attaining operating temperatures of ∼20 K for the optics and 30–50 K for the detector. A thermal leak near the detector focal plane prevented dark current measurements with this instrument. Instead, operations with MIRAC-5 focused primarily on characterizing the detector's linearity, gain, and excess noise properties under illumination.

3.2 | MITTEN testing at MI

The Michigan Infrared Test Thermal ELT N-band (MITTEN) Cryostat was used to test GeoSnap from the spring of 2020 through the summer of 2021 (Bowens et al. 2020). The MITTEN optical bench can reach temperatures <20 K with interior surfaces reaching ∼40 K enabled with a two-stage pulse-tube cryocooler package from Cryomech. It has an internal working volume of 0.128 m^3. To minimize external leaks and stray light, MITTEN does not have a window for light to enter from the outside; instead, an internal light source has been installed. The detector mount is a molybdenum block attached to 6061 aluminum stand mounted on the optics plate. The detector temperature can be controlled on to ±0.001 K within 30–70 K. A minimum temperature of 35 K and a maximum temperature changing rate are enforced to protect the detector.

MITTEN also includes an internal blackbody source, filter wheel, and pinhole point sources paired with an Offner relay to perform measurements of quantum efficiency and response to point sources relative to thermal background. However, this work focuses primarily on taking advantage of the cryostat's cold and dark interior to measure dark current, ROIC glow, read noise, and confirming the excess noise profiles of the GeoSnap device in a different operating environment.

4 | GEOSNAP CHARACTERIZATION

A single quadrant of the full GeoSnap 2048 × 2048 ROIC (18-μm pixels) was hybridized to a longwave HgCdTe material with sensitivity extending past ∼13 μm. The die material bonded to this device comes from the same wafer as H1RG-18508 characterized in Cabrera et al. (2019) and should have similar properties, such as cutoff wavelength, quantum efficiency (QE), and intrinsic dark current.

Unless otherwise specified, reported values refer to the `A0` ROIC operating in low gain mode (large well depths) with an applied detector reverse bias of 130 mV. Table 1 summarizes the main features of the detector, while Figure 3 highlights representative images for the detector bias, flat field illumination pattern, detector well level, and dark current distributions.

4.1 | Quantum efficiency

Figure 4 shows the wavelength-dependent QE measurements of the process evaluation chip (PEC) at T = 30 K provided by TIS, overplotted with a typical atmospheric transmission curve. The hybridized quadrant of the GeoSnap device has a wavelength sensitivity ranging approximately between 1 and 13.5 μm, covering the JHKLMN atmospheric windows. The average QE at 10 μm is ∼0.7 with a longwave half-power point corresponding to a cutoff of 12.75 μm. For higher operating temperatures, we expect this cutoff to decrease slightly. The CdZnTe substrate on this device has not been thinned, nor has an anti-reflection coating been applied to the surface, implying QE > 0.9 for science-grade devices. CdZnTe thinning should further extend the short-wavelength roll-off to below 1 μm.

4.2 | Linearity

Three sets of linearity data were acquired at a temperature of 45K while operating the detector with a frame rate of 85 Hz: 1) at Teledyne with all four quadrants powered, 2) at Arizona with all four quadrants, 3) again at Arizona with the three bare ROIC quadrants powered down. For

TABLE 1 Device performance summary

Specification	GeoSnap-18	AQUARIUS[a]	GeoSnap comments
Array size	2048 × 2048	1024 × 1024	Only 1k × 1k active; available in 1, 2, or 3 k formats
Pixel size	18 μm	30 μm	
Operating temperature	35–50 K	7–9 K	Absolute lower limit not characterized in this study
Max full frame rate	86.7 Hz	100 Hz	120–140 Hz in special configuration
Wavelength range	1–13 μm	3–28 μm	Can range 0.4–15 μm, depending on HgCdTe bandgap
Quantum efficiency	>70%	>40%	>90% with thinned CdZnTe and AR coating
Well depth	1.3 Me^-	0.8–1 Me^-	>2.5 Me^- for `B0` revision; 180 ke^- in high gain mode
Non-linearity	<5%	<5%	<0.1% up to full well after correction
Dark current (per pixel)	>10,000 e^-/s	<100 e^-/s	Measured at 38 K; limited by ROIC glow
Dark current density	>0.5 nA/cm^2	<0.002 nA/cm^2	
Read noise	140 e^-	200 e^-	~90% of kTC removed within unit cell processing
Excess noise	$1/f$	ELFN	Mitigated through chopping and slower readout speed
Power dissipation	1000 mW	250 mW	250–500 mW when operating only a single quadrant

Note: GeoSnap performance summary as measured in low gain mode and comparison to AQUARIUS characteristics.
[a]See Hoffmann et al. (2014), Ives et al. (2012), and Ives et al. (2014).

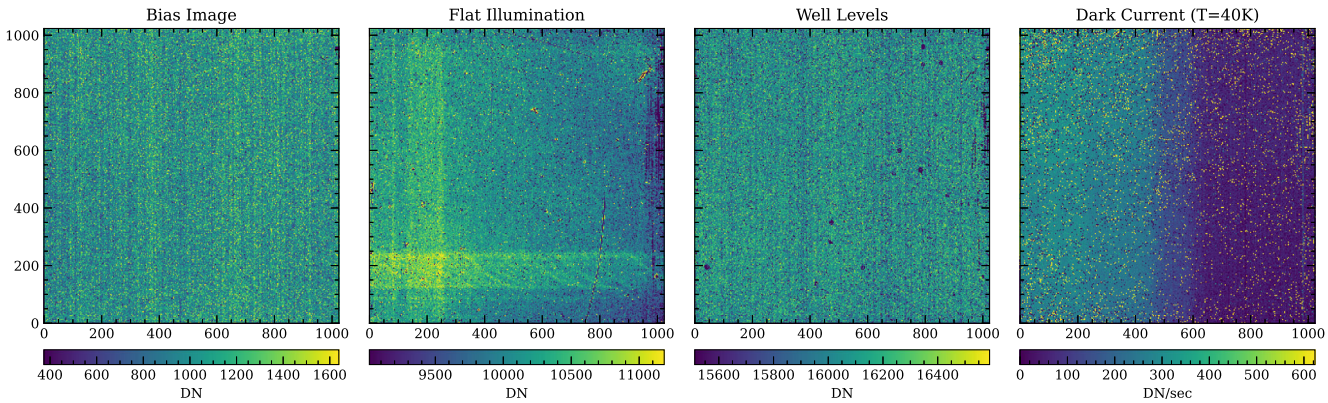


FIGURE 3 Representative images of the array image properties, including bias frame, flat field illumination, well level distribution, and dark current. The "plaid" stripe pattern in the Flat Illumination panel is consistently observed in different cryostats when the array is subjected to sufficient illumination, likely due to reflections from the bezel edges surrounding the hybridized region. The gradient in the dark current image likely relates to MUX glow.

each experimental setup, the input flux was held at a constant rate while changing the fractional integration time per frame, stepping in 5% intervals to increase the measured signal until saturation. At each step, 128 frames were acquired and averaged together.

Data were processed by first stacking the averaged frames into a single "ramp" data cube. A polynomial fit was subsequently performed on each pixel to calculate the zero-flux bias image for each of the three independent datasets. The detector bias offsets were then subtracted from their respective ramps.

Prior to testing, we tuned the FPM's internal biases and register to operate at low temperatures from 35 to 55 K. Part of this process included configuring the ADC gain to the recommended ~135 μV/DN such that the full range of the 14-bit ADC spans the 2.2 V input range. When including an ADC offset to capture minimum integration images near the detector reset level, pixel values become clipped at the top end of the digitizer before reaching natural saturation. Consequently, approximately 67% of pixels in saturated frames are railed at a value of 16,383 DN.

Figure 5 shows the median ramp data for each run as well as the small deviations from linearity as a function of signal level. Overall, the ramp data appear to be highly linear across the entire dynamic range with residuals of only a few percent. The fractional nonlinearity with

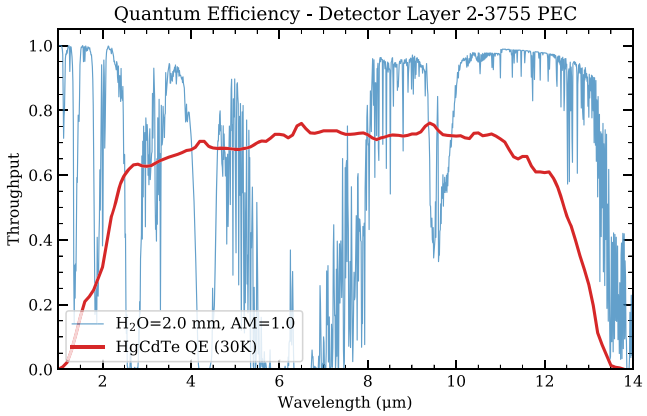


FIGURE 4 Quantum efficiency provided by TIS of process evaluation chip (T = 30 K) relative to ATRAN model with 2 mm of precipitable water vapor at an airmass of 1 (Lord 1992).

respect to signal level (bottom right panel of Figure 5) is well fit by a linear function with minor deviations at relative low-signal levels (<2500 DN). These deviations are shown to be repeatable between runs.

4.3 | Gain and well depth

Similar to the linearity data, a series of 128 frames were acquired at a given illumination level to measure effective gain. A variety of independent datasets were acquired at Teledyne and with the MIRAC-5 setup at Arizona. In addition to the three described in Section 4.2, we also analyzed a TIS evaluation dataset that held the fractional integration time constant while changing the total flux from an input blackbody device. In addition, we included a dataset similar to those in the previous section, but acquired at 38K with only the hybridized quadrant powered.

For a given illumination level, we calculated the average signal and variance for each pixel. After applying linearity corrections, the median values of these signal and variance images are plotted to generate the photon transfer curve (PTC) shown in Figure 6. The PTC curves for all datasets show significant consistency, indicating excellent repeatability between cooldowns. IPC corrections were not applied since this effect is absent from the GeoSnap device (Section 4.7).

We adopt gain of 83 e^-/DN, implying a median well depth of 1.3 Me^-/pixel for this device (Figure 7). Because pixel values get clipped at the top end of the ADC range before reaching saturation, the full well depth is likely slightly higher than measured. That is, reducing the DC offset would likely produce a wider sampling of the intrinsic well within the ADC's dynamic range. The normal distribution depicted in Figure 7 is due to pixel-to-pixel offsets in the frame bias, whereas raw data of a saturated frame would show a sharp cutoff at the equivalent of 16,383 DN. About 98.7% of pixels have well depths greater than 1.2 Me^-.

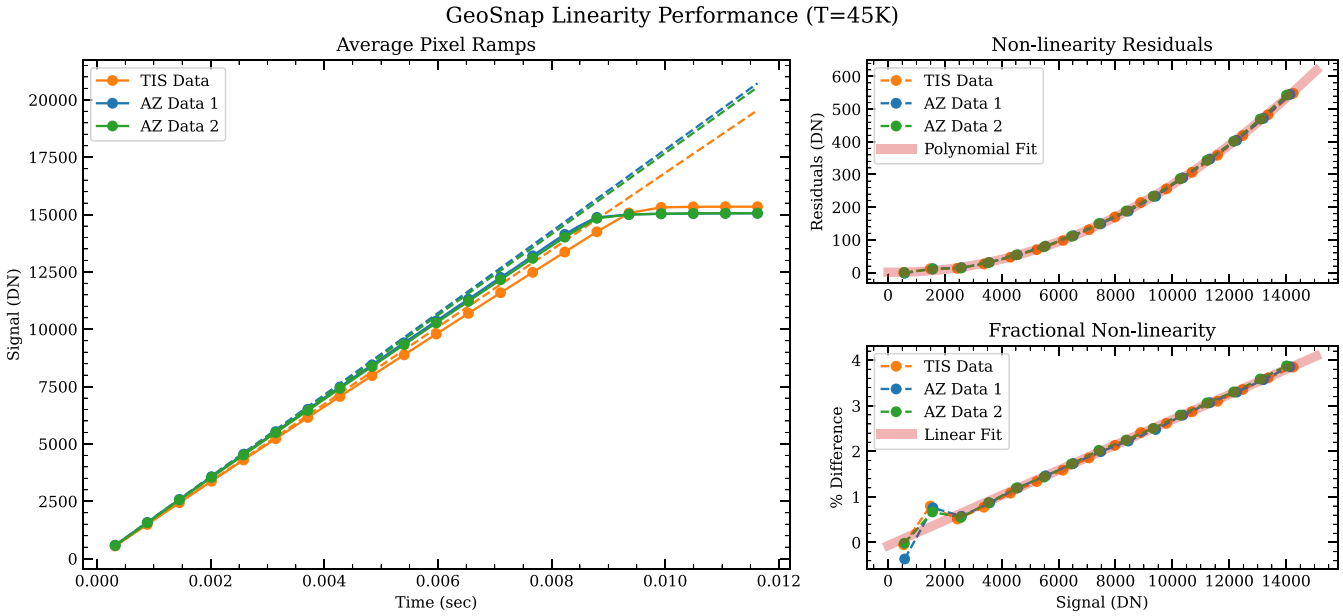


FIGURE 5 Linearity data acquired at 85 Hz frame rate with an operating temperature of 45 K for three independent linearity runs. *Left:* Average signal for successive integration settings corresponding to intervals of 5% of the total frame time; the two AZ overlap. *Upper right:* the residuals relative to the linear component of a polynomial fit. These are well fit with a polynomial that can be used to calculate expected residuals based on measured signal level. *Lower right:* Similar to above, fractional nonlinearity is linear with signal value.

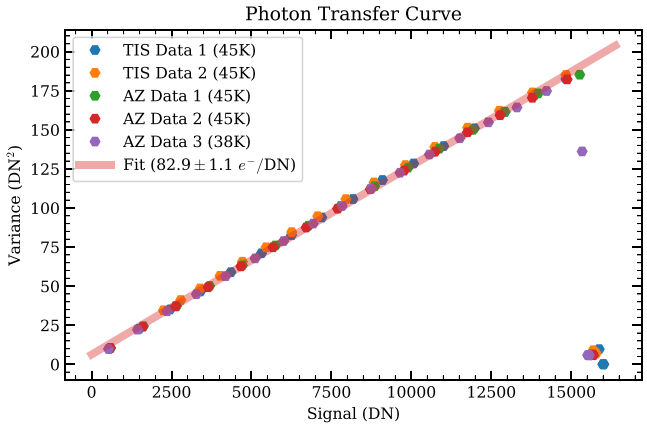


FIGURE 6 Resulting GeoSnap photon transfer curve for multiple datasets acquired in a variety of configurations and temperatures.

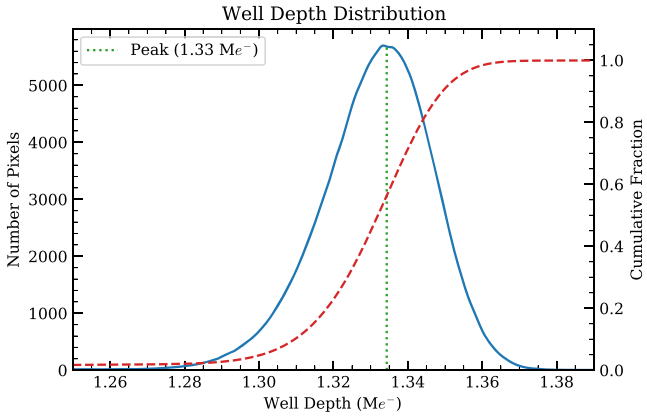


FIGURE 7 Histogram of well depths for all pixels hybridized quadrant of the GeoSnap device. The distribution peaks slightly above 1.3 Me^-.

4.4 | Dark current

Dark current datasets were acquired with the GeoSnap detector in the MITTEN cryosat at Michigan, which regularly achieved an ambient background temperature of $\lesssim$20 K. The combination of low radiative background and absence of optical input ports provides a true measure of the FPM's self-generated background flux.

Detector operating temperatures ranged between 38 K and 55 K, where minimum temperature was limited by self-heating of the FPM during operations (0.5–1 W of power, depending on operation mode). To minimize the effects of detector power output, data were acquired with a nominal frame rate of 10 Hz with a single hybridized quadrant. Operating at 10 Hz also provided the benefit of maximizing the photon collection time for sufficient signal to noise.

For a given temperature setting, the fractional integration parameter, t_{frac}, was stepped over a range of 0–1 in 0.05 increments. At each step, 128 contiguous frames were recorded and median combined after correcting for residual bias offsets between frames. All pixels within the resulting ramp data cube were fit with a linear function to produce a dark current slope image, one for each temperature setting (Figure 8).

The resulting slope images exhibit two flux components roughly split between the left and right halves of the array, particularly evident at the lower temperatures. It seems unlikely that intrinsic dark current alone contributes to the bimodal distribution, which is instead likely caused by photon sources internal to the FPM. Incidentally, these two halves correspond to separate output data streams with independent preamps and ADCs. The two distributions converge as the operating temperature increases, suggesting detector dark current becomes more prominent. We measure a minimum dark current rate of ~6.6 ke^-/s, which corresponds to the peak of the distribution of the right side of the 38 K slope image. The images in Figure 8 also demonstrate an increase in the number of high dark current pixels with temperatures.

This GeoSnap device does not exhibit the crosshatching pattern attributed to the growth process of the HgCdTe crystal lattice structure because of the applied low bias while operating at a temperature where thermal dark currents dominate. In general, the crosshatching pattern becomes apparent for low thermal dark currents along with an applied bias sufficiently high enough to produce significant tunneling dark current in pixels with defects associated with the lattice mismatch. Such patterns were shown in the LW13 H1RG arrays characterized in Cabrera et al. (2019) and have been reported in a number of other publications (e.g., Chang et al. 2008; Martinka et al. 2001; Schlawin et al. 2021).

4.4.1 | Dark Current Models

Dark current behavior for HgCdTe arrays is parameterized in Tennant et al. (2008) through the empirically derived "Rule 07" formula, which can be used to generally predict dark current performance for this material based solely on the cutoff wavelength and operating temperature. While Rule 07 predictions hold for a range of temperatures and cutoff wavelengths, the performance can be exceeded by optimizing of the fabrication process and device structure. We plot the Rule 07 relationship in Figure 9 assuming a 12.75-μm cutoff corresponding to the GeoSnap device. At temperatures >45 K, our measured dark current falls below this relationship.

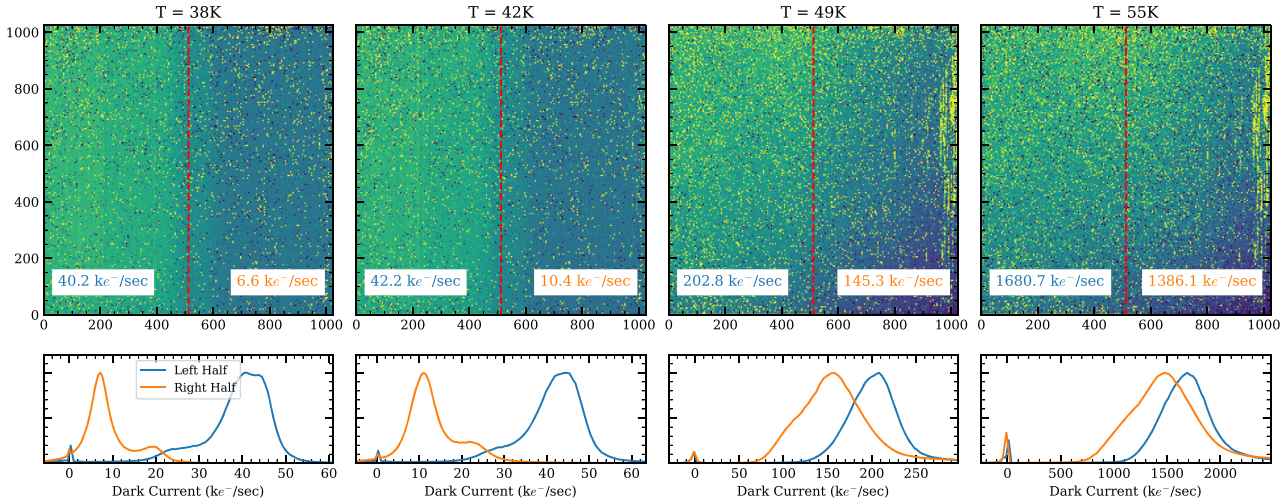


FIGURE 8 A sample of dark current slope images acquired at 10Hz framerate in the MITTEN cryostat, demonstrating the evolution of background rates for increasing temperature. Lower figures are histograms of the left and right halves of each slope image. For lower temperatures, there is a clear difference between the two halves, which converges as temperature increases.

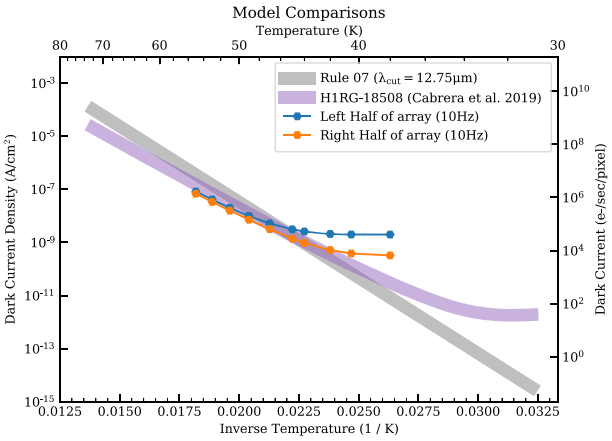


FIGURE 9 Arrhenius plot of measured GeoSnap dark current densities at 130mV reverse bias compared to "Rule 07" (Tennant 2010; Tennant et al. 2008) and H1RG-18508 model fit (fig. 18 of Cabrera et al. 2019). GeoSnap values at T > 45 K are consistent with those measured for the H1RG part, with values at lower temperatures flattening due to background radiation (e.g., MUX glow).

In addition, Figure 9 shows the dark current model derived from the H1RG-18508 array data presented in Cabrera et al. (2019), which incorporates die material originating from the same HgCdTe wafer as this GeoSnap device. The dark current model incorporates three primary mechanisms: band-to-band tunneling, generation-recombination (GR), and diffusion. At T > 35 K, diffusion and GR dominate the H1RG data, while band-to-band tunneling is the primary contributor at T < 35 K.

The GeoSnap measurements follow the H1RG-based model fairly well for temperatures greater than 45K. The primary deviation occurs at the inflection point where the GeoSnap dark current behavior flattens at lower temperatures, potentially attributed to different operating modes or additional sources of background signal. For instance, the H1RG operated with reverse bias of 275 mV compared with 130 mV for the GeoSnap, and the GeoSnap utilizes a much higher readout speed with on-chip ADC and consequently larger power dissipation.

Because diffusion and GR dark currents do not change considerably with bias in this regime, good agreement between the GeoSnap and H1RG data at T > 45 K suggests consistent characteristics between detectors for these two contributors. In addition, current from band-to-band tunneling (dominant at lower temperatures) is expected to drop for GeoSnap's lower reverse bias, implying that the observed flattening to the GeoSnap curves at T ∼45 K arises from a different source. Combined with the distinct differences between the left and right half of the GeoSnap array, these deviations are likely explained by the FPM power dissipation, or multiplexer (MUX) glow. The GeoSnap's HgCdTe material therefore appears to have intrinsic dark current consistent with the model derived for the H1RG-18508, which is expected given they are two of the four die from the same growth wafer.

4.4.2 | MUX glow

Measurements of dark current typically include additional background emission as the two are not easily distinguishable. In particular, mid- and longwave detectors are susceptible to self-generated emission (Tam & Hu 1984), which can be significant compared with the actual dark current of the photosensitive material. Previous studies of

HxRG detectors have attributed anomalously high dark current to thermal excitation within the multiplexer unit cell rather than a process intrinsic to HgCdTe layer (Cabrera et al. 2019).

For the 5-μm detectors aboard JWST, this "MUX glow" relates directly to the current supplied to the pixel source follower (Regan & Bergeron 2020). Increasing the current induces local heating within a pixel's unit cell during the sampling process, which is then measured as infrared radiation, especially by material with longer wavelength cutoff. Further, operating these detectors in subarray witnessed an increase in the glow due to a given pixel being addressed at a higher frequency. That is, sampling the pixel more often accumulates additional glow before prior local heating is able to fully dissipate. Compared with H1RG and H2RG data, we suspect that the GeoSnap's measured dark current floor at lower temperatures is MUX glow due to the large on-chip power consumption.

4.5 | Read noise

In this section, we report the read noise for the GeoSnap's standard single-frame readout. The GeoSnap ROIC provides an on-chip CDS subtraction that occurs within the normal pixel sampling process, reducing the kTC reset noise contributions by up to 90% (private communication, TIS). We assess the read noise performance as a function of operating temperature and frame rate.

To compute the read noise, 128 consecutive frames were acquired under dark conditions for a variety of reset times, frame rates, and temperatures in low gain mode. The RMS noise per pixel was calculated for each configuration. Due to relatively large background signals relative to intrinsic read noise, the photon signal variance was estimated from the frame averages, and then subtracted in quadrature from the measured total noise to obtain the read noise values per pixel.

The left panel of Figure 10 shows a histogram of the pixel noise operating at 45 K with a frame rate of 85 Hz. Read noise for a typical single frame in the low gain mode is measured to be approximately 140 e^- RMS, corresponding to the peak of the histogram, whereas the median is slightly higher (~150 e^-) due to the extended tail of the distribution. For this particular device, noise appears to increase slightly as the detector operating temperature decreases, although the change is a mere 7% over ~10 K. The low temperature increase may be related to the photon noise subtraction, over-correcting for larger signal values or under-correcting at lower signal values. There is also

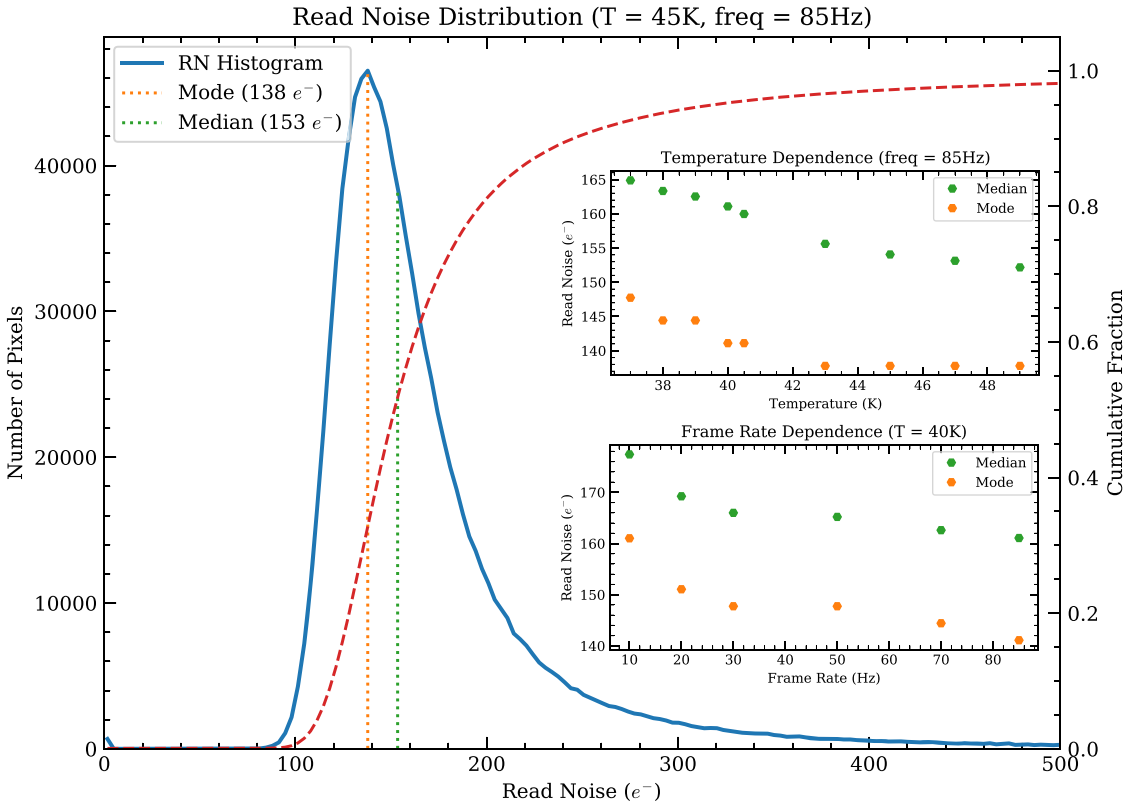


FIGURE 10 Detector read noise distribution for typical operating parameters of 85 Hz frame rate at 45 K temperature, as a function of temperature (top inset) and frame rate (bottom inset).

evidence for temperature-dependent read noise in H2RGs (private communication, JWST NIRCam team).

Similarly, the read noise is observed to increase toward lower frame rates. The rise may be due to larger contributes from $1/f$ noise component (Section 5) for larger sampling intervals.

4.6 | Persistence

Our test environments did not include a mechanism for effectively measuring latent signals related to detector persistence. Regardless, we were unable to visually identify any obvious evidence of persistence in our data when switching between partially saturated frames and dark frames. This is not unexpected, given the combination of the CTIA pixel cell held at a constant voltage, high-speed readout inhibiting build-up of charge within traps, and the long wavelength cutoff where persistence tends to be reduced compared with shorter wavelength devices (Leisenring et al. 2016).

4.7 | IPC

We used dark data presented in Section 4.4 to assess the presence of interpixel capacitance (IPC; Moore et al. 2004). By selecting isolated hot pixels with excessively high dark current rates, we can determine the coupling between these pixels to their nearest neighbors. We isolated ~8300 hot pixels, removed their surrounding background levels, and then normalized the total signal within the 3×3 region surrounding the hot pixels to a value 1. After stacking and median-combining the normalized image, we calculate a coupling constant $\alpha_{ipc} = 0.001 \pm 0.005$, which is consistent with 0. This is expected, because the CTIA readout circuit holds the pixel gates at the same constant voltage, which is predicted to remove the effects of capacitive coupling between neighboring pixels.

4.8 | Operability

This engineering-grade array shows few cosmetic defects as exhibited in the images in Figure 3. Even though flat field illuminated image shows significant nonuniformity, this pattern is consistent and easily removed through standard data reduction processes.

We calculate the fraction of operable pixels by measuring the total number of pixels with acceptable read noise, dark current, and well depths at an operating temperature of 40 K. Figure 11 shows the distribution of pixels for a histogram image of dark current versus well depth. Following the data presented in Sections 4.3 and 4.4, the distribution is centered near a dark currents of 40 ke$^-$/s and 1.3 Me$^-$ well depth. Approximately 95% of pixels have dark currents below 10^5 e$^-$/sec, well depths of >1.25 Me$^-$, and read noise values less than 500 e$^-$. We expect the number of inoperable pixels to increase with temperature, as evidenced in Figure 8.

5 | EXCESS NOISE ANALYSIS

Excess low-frequency noise (ELFN) is a property of previous generation of Si:Sb Blocked Impurity Band (BIB; Stapelbroek et al. 1984) and Si:As Impurity Band Conduction (IBC; Arrington et al. 1998) detectors used for longwave infrared astronomy. ELFN is produced within the detector material, specifically resulting from additional photon absorption within the IBC blocking layer. This behavior prevents the noise from reducing as the square root of the number of reads, especially in high-flux regimes. This effect has been widely reported in Raytheon AQUARIUS Si:As arrays (e.g., Hoffmann et al. 2014; Ives et al. 2012; Ives et al. 2014), but should be absent in the GeoSnap's HgCdTe detector material owing to the different material and unit cell architecture.

As expected, the GeoSnap's pixel noise power spectrum does not exhibit the characteristic ELFN profile observed in the AQUARIUS array. However, the noise power spectrum instead shows a prominent and troubling $1/f$ profile (Figure 12). We identified multiple sources of $1/f$ noise common to the rows, columns, and full array, which are readily subtracted during standard data reduction processes. However, a significant residual $1/f$ component remains as it cannot be removed through common mode analysis (e.g., subtraction of neighboring pixels). For dark observations operating at 85 Hz frame rate, the $1/f$ component dominates over the underlying Gaussian noise on timescales longer than ~1 s (frequencies below ~1 Hz). In addition, the slope of the $1/f$ component does not always scale exactly with frequency. Instead, its power spectrum has the functional form,

$$S(f) \propto f^{\alpha}, \tag{1}$$

where the exponent, α, has a best-fit value that varies between −1 and −1.5.

5.1 | Frame rate and integration time

We acquired a number of data sets with changing frame rates to assess any modulation of the $1/f$ noise. Figure 13 demonstrates that the position of the $1/f$ component

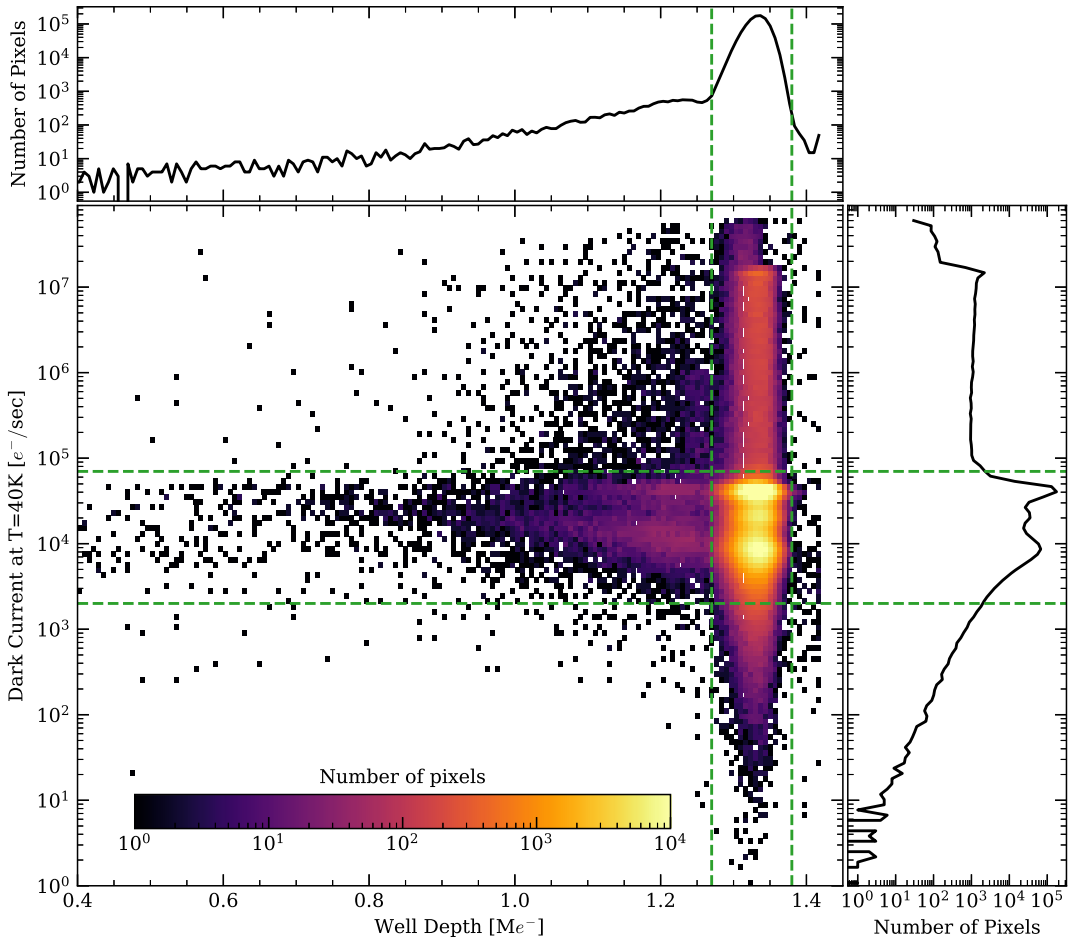


FIGURE 11 2D histogram of dark current versus well depth obtained with a focal plane temperature of 40 K. The distribution is centered at 40.4 ke^-/s and 1.33 Me^-. Approximately 88% of pixels reside within the dashed rectangular region surrounding the peak of the distribution.

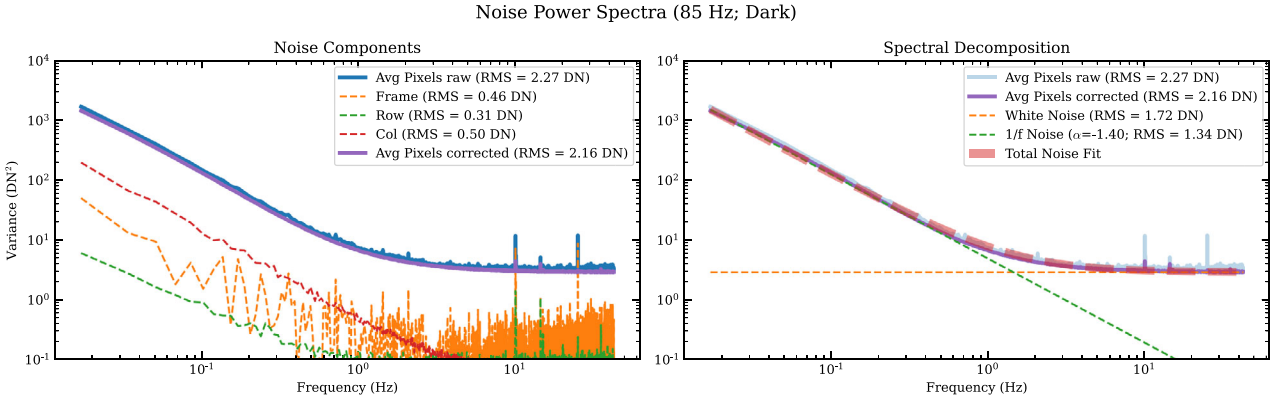


FIGURE 12 *Left:* Average pixel noise power spectrum in units of variance (DN^2) before and after removal of correlated components (frames, rows, columns) for a sequence of 5000 dark observations. Data were acquired at a frame rate of 85 Hz and temperature of 40 K. *Right:* Final noise profile fit breaking out white noise and $1/f$ noise components. In this case, the $1/f$ component has a best-fit exponent of $\alpha = -1.4$.

within the power spectrum directly correlates with the frame rate. That is, the power spectra for different frame rates and their $1/f$ components perfectly overlap when plotting with respect to the frequency on a "per frame" basis rather than with respect to Hz (lower panel of Figure 13). This suggests that this noise must originate from an internal process that does not depend on frame rate. As a consequence, observations with lower

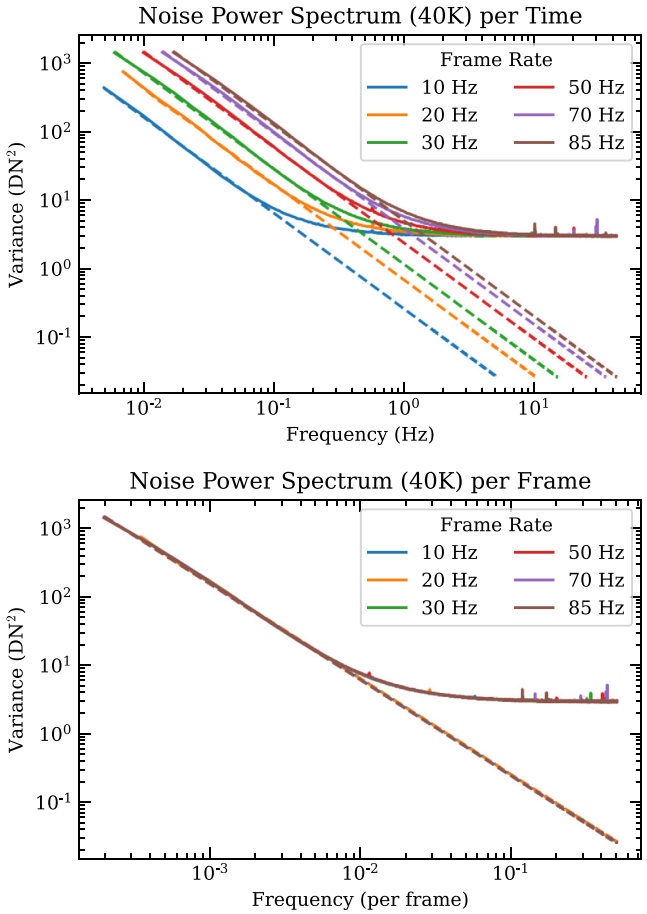


FIGURE 13 The noise power spectra of dark observations acquired at different frame rates. The upper panel shows the power spectrum for each data set plotted as a function of temporal frequency, whereas the same data are plotted in the lower panel as a function of "per frame" (i.e., dividing the values of each curve by their corresponding frame rate). Dashed lines indicate individual fits to the $1/f$ component.

framerates will have effectively less $1/f$ noise contributions for a fixed period of time.

In addition, we checked for dependency of $1/f$ profile on the fractional integration time. The GeoSnap provides the ability to control the fraction of a frame time that is dedicated to integration by configuring the duration of the pixel cell reset switch. For both dark and half-well observations, the $1/f$ noise profile did not change with respect to the fractional integration time.

5.2 | Signal level

This noise profile is also observed within the nonhybridized quadrants of the array with the same characteristics as dark observations in the hybridized quadrant, indicating the $1/f$ noise arises somewhere within the pixel cell's readout chain. Unlike the AQUARIUS arrays, this is

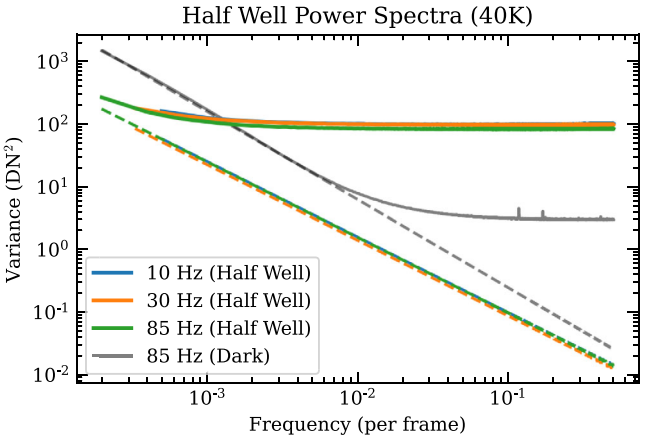


FIGURE 14 Comparison of power spectrum observed at 50% well fill for a range of frame rates plotted as a function of frame frequency, following the lower panel in Figure 13. Dashed lines indicate the fitted $1/f$ component. The power spectrum for a dark observation is provided for reference, showing that half-well observations produce significant reduction in $1/f$ component both absolutely as well as relative to the white (photon) noise.

not a phenomenon related to the HgCdTe detector material, which would have likely been identified in previous HxRG devices.

While this level of noise would be challenging for low-flux applications, the absolute contributions from the $1/f$ component appear to lessen with increased signal levels. Figure 14 shows that the noise properties are significantly improved when the device is uniformly illuminated to a 50% well level compared with dark observations. The $1/f$ noise is reduced and the slope is less steep with a best-fit exponent of $\alpha = -1.2$, suggesting that signal levels somehow affects manifestation of the $1/f$ noise. Combined with the overall increase of photon noise, these two effects favorably conspire to push the upturned knee of the observed power spectrum profile to much lower frequencies. Observations with high-background rates then become tractable through moderately slow chopping and/or nodding of the telescope, allowing an observer to re-position their source within the detector's FoV on manageable timescales without significant overhead.

Figure 15 compares the noise scaling as a function of consecutively averaged frames for dark and half-well illuminated scenarios for both the GeoSnap and AQUARIUS arrays. The AQUARIUS data were acquired using the LBTI/NOMIC instrument (private communication, S. Ertel). For each scenario, we obtained 2000 consecutive frames, subtracted the average relative offsets between frames to remove any electronic bias offsets, and generated bad pixel masks. Each sequence of images was then split into first and second halves (as would be experienced for a telescope nod offset), which were subtracted

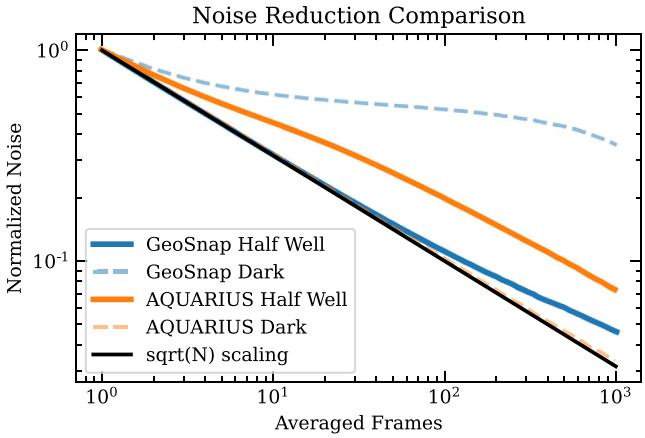


FIGURE 15 Noise reduction as a function of number of averaged frames, comparing GeoSnap with LBTI/NOMIC's AQUARIUS data for dark and half-well signal scenarios.

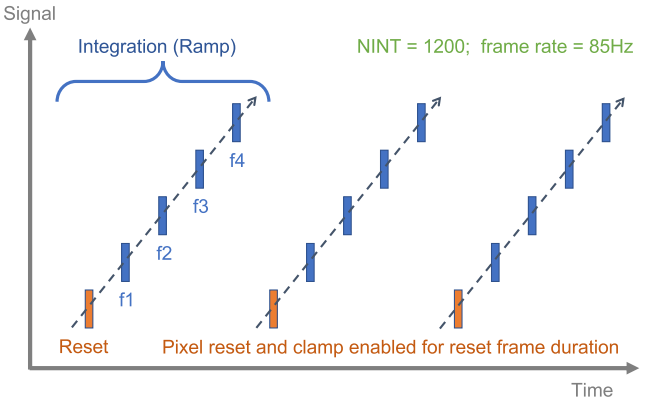


FIGURE 16 An illustration of the up-the-ramp readout scheme implemented to investigate $1/f$ noise as a function of signal levels. Each integration consists of a single reset frame and four nondestructive read frames. All frames, including the reset frames, are written to disk.

frame-by-frame, leaving a sequence of noise images. We then successively averaged together the differenced images and measured the resulting noise after applying a bad pixel mask.

In Figure 15, we recover the ELFN behavior of LBTI/-NOMIC's AQUARIUS array, where the noise drop-off for dark observations very closely follows the ideal $\sqrt{N}$ scaling, but higher well depths produce a large noise excess. GeoSnap's $1/f$ behavior is effectively the inverse of ELFN with respect to signal. For the dark observations case, our chosen frame subtraction baseline (1000 frame times) means that the $1/f$ contributions become the dominate noise source, preventing efficient reduction of the noise through frame averaging. Instead, the low-signal scenario would require subtraction of frames pairs much closer in time. At high signal levels, though, there is a ~40% noise excess (compared to 250% for the AQUARIUS), which only improves with higher well depths; GeoSnap is the more favorable device in high-flux regimes.

5.3 | Temperatures

A number of $1/f$ noise observations were acquired for a range of temperature between 38 and 52 K in both dark and half-well configurations. The power spectrum profiles for the two well level settings were consistent across temperatures. We conclude that the amplitude and α value of the $1/f$ excess noise does not depend on temperature.

5.4 | Sample up the ramp

In general, $1/f$ noise can be conceptualized as a slowly varying pixel offset whose distribution is non-Gaussian and power spectrum follows the form in Equation (1). Sampling this signal multiple times before it significantly changes allows one to effectively remove the $1/f$ contribution. That is, subtracting consecutive frames will effectively eliminate the $1/f$ component, resulting in primarily white noise residuals. If the source of this noise were simply a slowly varying DC offset, then a readout scheme implementing correlated double sample (CDS) or sample-up-the-ramp (SUR) readout should remove it, assuming sampling is fast enough.

We implemented a custom firmware to acquire SUR data (Figure 16). This mode deactivates the internal on-chip CDS subtraction, holds the pixel reset switch closed on the "zeroth" frame, and then nondestructively reads some number of frames as the on-chip capacitor continues to accumulate charge until the next reset frame. Our ramp integrations consisted of one reset frame and four read frames, which are written to disk as a separate file per frame. Data were acquired at 85 Hz with 1200 integrations (e.g., 6000 total frame). The average well level in the final read frame was approximately 90%. As a control, we simultaneously acquired MUX data from a bare quadrant when evaluating the behavior of the hybridized quadrant.

Under dark conditions, performing ramp fitting as well as last-minus-first read subtraction completely removed the 1/f component in both the hybridized and ROIC quadrants (Figure 17). While encouraging, results from Section 5.2 indicated that $1/f$ noise profile can be affected by the accumulated signal. Indeed, when illuminating the detector, a significant residual $1/f$ component exists after performing intra-ramp frame subtraction. The amount of residual $1/f$ directly relates to initial signal differences between the frames. For instance, $R_4 - R_3$ performs better in this regards than $R_4 - R_1$. The paradigm of a single

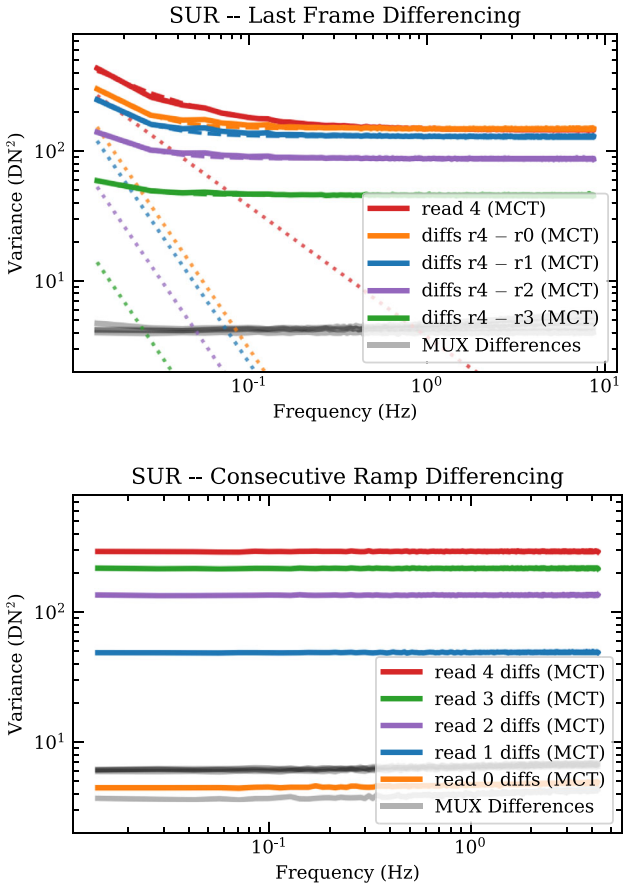


FIGURE 17 *Upper:* Power spectra for SUR data processed in various manners. The colored lines indicate subtraction of some frame within the ramps from the final read frame. Dashed lines are the fitted $1/f$ components. Frame pairs with larger signals differences reveal larger residual $1/f$ noise after subtraction. Whereas the MUX data acquired at the same time (in a nonhybridized quadrant with no charge accumulation) show complete removal of the $1/f$ component, presumably because the data have the same signal levels. *Lower:* Differences of the same read frames in consecutive integrations. Since all images for the same read frame have similar signal levels, the $1/f$ component is always removed.

$1/f$ signal propagating through consecutive reads appears to be incomplete. Instead, the $1/f$ component appears to be modulated by the accumulated charge in some manner. This is an active area research by Teledyne to isolate the source and mitigate this electronic noise.

To further highlight this signal dependency, subtracting the same read frame in subsequent ramps completely removes the $1/f$ noise component; the power spectra are perfectly flat, consistent with Gaussian noise (Figure 17, lower panel). We additionally attempted subtracting various combinations of frame pairs, but the only scenarios that completely removed the $1/f$ noise component required equal signal levels for the non-consecutive subtraction pairs.

5.5 | Mitigation strategies

In order to better isolate the source of the $1/f$ noise within the readout chain, we generated a few data sets that turned off various components within the unit cell. So far, we have shown that the noise cannot originate from the HgCdTe material (present in both MUX and active pixels) or the CDS functionality (CDS was turned off during the ramp sampling procedure). We further attempted to isolate the CTIA by always keeping the CDS clamp switch closed as well as setting the CTIA bias to 0 nA. In both cases, the $1/f$ noise was still present at the same levels. Hence, it appears that the noise does not originate in the CTIA circuit, but must originate in components after the CTIA and prior to (or during) A/D conversion.

The latest `B0` ROIC revision qualitatively shows the same $1/f$ noise contamination (private communication, D. Ives), meaning that instruments employing these devices require mitigation strategies until such time that the source of the noise is isolated and removed in future firmware or hardware updates.

We have identified a number of observing strategies that will help reduce or $1/f$ noise contributions:

1. Operate close to full well. For high-background observations, the new ROICs come equipped with larger well depths of ~2.4–2.6 Me^- allowing photon noise to dominate over the $1/f$ noise component (Figure 14).
2. Operate at lower frequencies. Since the $1/f$ noise profile is generated per frame rather than per Hz, operating at lower frame rates effectively shifts $1/f$ noise to lower frequencies and reduces, allowing more efficient nodding (Figure 13).
3. Perform chopping and/or nodding. The $1/f$ noise can be effectively removed by subtracting pairs of observations where the source has been modulated via tip/tilt offsets faster than the characteristic frequency corresponding to the up-turn of the $1/f$ noise component. This strategy will be implemented in the ELT/METIS instrument (Brandl et al. 2022; Paalvast et al. 2014).
4. For low-background observations, a CDS or SUR mode may provide an effective way to subtraction out the $1/f$ noise if signal accumulation is low. This work did not investigate GeoSnap's high gain mode, which may be more suitable for such a scenario.

6 | CONCLUSIONS

We performed testing and characterization of the first mid-IR GeoSnap-18 device produced specifically for ground-based astronomy. This engineering-grade part

consisted of an early A0 ROIC hybridized with a 13-μm HgCdTe die onto a single 1024×1024 quadrant. The photosensitive region was not AR-coated and retained its CdZnTe substrate, limiting QE to $\lesssim$70%.

The device was found to have the following properties while operating in low gain mode:

- The GeoSnap showed a well depth of ∼1.3 Me^- with a gain of 83 e^-/DN. We were unable to probe the full range of the well depth due to hitting the upper limit of the ADC.
- The pixel response showed a well-behaved nonlinearity with a ∼4% maximum deviation from linear at the highest signal levels.
- Dark current measurements at T > 45 K were consistent with HgCdTe models derived for H1RG detectors bonded to similar HgCdTe material. Measurements below 45 K were limited by MUX glow, flatting out with a lower limit of 6600 e^-/s.
- The detector read noise is measured to be approximately 140 e^- RMS, corresponding to the peak of the histogram, whereas the median is slightly higher (∼150 e^-) due to distribution's extended tail.
- Approximately 95% of pixels have dark currents below 10^5 e^-/s, well depths of >1.25 Me^-, and read noise values less than 500 e^-.
- We did not find any evidence for persistence or IPC in the gathered GeoSnap data.

While we confirmed the GeoSnap array is free of ELFN, it instead suffers from a $1/f$like noise originating within the pixel readout. This noise severely limits sensitivity in low-signal regimes and can dominate on timescales greater than a couple of seconds for the fastest frame rates. We observed the following behaviors:

- The power spectrum for dark observations operating at 85 Hz frame rate was dominated by $1/f$ component on timescales greater than ∼1 s.
- The $1/f$ power spectrum profile was observed to shift with frame rate such that $1/f$ components always exhibited the same power spectrum when plotted with respect to a "per frame" frequency.
- Observations acquired at half well showed a lower overall $1/f$ contribution along with a more shallow slope compared with dark observations.
- Analysis of SUR observations showed that a residual $1/f$ contribution remained after subtracting consecutive frames with different signal levels. However, subtracting frames with the same accumulated signal from consecutive ramp integrations completely removed the $1/f$ component. These results suggest the $1/f$ component is modified by signal level.
- GeoSnap's detector noise averages down much more favorably at high signal levels compared with the AQUARIUS array.
- We had determined that the source of the $1/f$ noise does not originate within the CTIA or CDS circuit, but must occur prior to or during the A/D conversion.

There are a few possible methods to mitigate the effect of the $1/f$ noise:

1. implement fast chopping to modulate the location of an astronomical source on the detector.
2. reduce the speed of the detector frame rate to shift the $1/f$ power spectrum to lower frequencies.
3. operate in a high-background environment where photon noise dominates over $1/f$ noise.

Despite the engineering-grade qualities of the device presented in this work, this detector is well-suited to perform high-quality mid-IR observations with ground-based instruments in high-background regime. The large well depths and high-speed frame rate provide significant advantages over HxRG arrays with similar cutoff wavelengths, while the noise properties have favorable performance relative to the Raytheon AQUARIUS array especially for high signal levels. Near-term work includes commissioning the GeoSnap array mounted in the MIRAC-5 camera while deployed behind the MAPS AO system on the MMT.

New science-grade devices will take advantage of double the well depths in the B0 ROICs as well as higher overall QE from AR-coated and CdZnTe-thinned surfaces (e.g., METIS; Brandl et al. 2022). Future design and engineering work is needed to isolate the origin of the $1/f$ noise as well as mitigate the MUX glow limiting the background dark rate.

ACKNOWLEDGMENTS

We thank the anonymous referee for their review, which has improved the quality of the paper and helped clarify several details. This work was supported through funding by the Templeton World Charity Foundation under grant TWCF0330 and Heising-Simons Foundation under grant 2020-1699. We thank Dr. Steve Ertel and the LBTI/-NOMIC team for loan of their AQUARIUS noise data, and are grateful for the engineering staff at Steward Observatory, The University of Arizona including Manny Montoya, Grant West, and Dennis Hart. We are also grateful for the collaboration of our colleagues at the

University of Michigan Department of Physics, in particular Dr. John Monnier, Megan Morgenstern, and Paul Thurmond and his team in Randall Laboratory, the Space Physics Research Lab, and the Plasmadynamic and Electric Propulsion Lab.

ORCID

Jarron M. Leisenring https://orcid.org/0000-0002-0834-6140
Dani Atkinson https://orcid.org/0000-0001-8589-1938
Rory Bowens https://orcid.org/0000-0003-0949-7212
Michael R. Meyer https://orcid.org/0000-0003-1227-3084
Mario S. Cabrera https://orcid.org/0000-0002-6621-8921
Alexandra Z. Greenbaum https://orcid.org/0000-0002-7162-8036
Philip Hinz https://orcid.org/0000-0002-1954-4564
William J. Forrest https://orcid.org/0000-0001-8192-0818
Craig W. McMurtry https://orcid.org/0000-0003-1969-4324
Judith L. Pipher https://orcid.org/0000-0002-0628-9605

REFERENCES

Arrington, D. C., Hubbs, J. E., Gramer, M. E., & Dole, G. A. 1998, in: *Proc. SPIE*, Vol. *3379*, 361. https://www.spiedigitallibrary.org/conference-proceedings-of-spie/3379/0000/Impact-of-excess-low-frequency-noise-ELFN-in-Si-As/10.1117/12.317603.short

Beckers, J. M. 1993, *ARA&A*, *31*, 13.

Beichman, C., Barrado, D., Belikov, R., et al. 2019, *BAAS*, *51*(3), 58.

Beletic, J. W., Blank, R., Gulbransen, D., et al. 2008, in: *Proc. SPIE*, Vol. *7021*, 70210H. https://www.spiedigitallibrary.org/conference-proceedings-of-spie/7021/1/Teledyne-Imaging-Sensors--infrared-imaging-technologies-for-astronomy-and/10.1117/12.790382.short

Boccaletti, A., Lagage, P. O., Baudoz, P., et al. 2015, *PASP*, *127*(953), 633.

Bowens, R., Leisenring, J., Meyer, M., et al. 2022, in: *Proc. SPIE*, Vol. *12184*, 121841U. https://www.spiedigitallibrary.org/conference-proceedings-of-spie/12184/2628953/MIRAC-5--a-ground-based-mid-IR-instrument-with/10.1117/12.2628953.short.

Bowens, R., Meyer, M. R., Delacroix, C., et al. 2021, *A&A*, *653*, A8.

Bowens, R., Viges, E., Meyer, M. R., et al. 2020, in: *Proc. SPIE*, Vol. *11447*, 1144737. https://www.spiedigitallibrary.org/conference-proceedings-of-spie/11447/2562995/The-Michigan-infrared-test-thermal-ELT-N-band-MITTEN-cryostat/10.1117/12.2562995.short

Brandl, B. R., Bettonvil, F., van Boekel, R., et al. 2022, in: *Proc. SPIE*, Vol. *12184*, 1218421. https://www.spiedigitallibrary.org/conference-proceedings-of-spie/12184/2628331/Status-update-on-the-development-of-METIS-the-mid-infrared/10.1117/12.2628331.short

Cabrera, M. S., McMurtry, C. W., Dorn, M. L., Forrest, W. J., Pipher, J. L., & Lee, D. 2019, *J. Astron. Telesc. Instrum. Syst.*, *5*, 036005.

Cabrera, M. S., McMurtry, C. W., Forrest, W. J., Pipher, J. L., Dorn, M. L., & Lee, D. 2020, *J. Astron. Telesc. Instrum. Syst.*, *6*, 011004.

Carter, A. L., Hinkley, S., Kammerer, J., et al. 2022, *arXiv e-prints*, arXiv:2208.14990.

Chang, Y., Becker, C. R., Grein, C. H., et al. 2008, *J. Electron. Mater.*, *37*(9), 1171.

Danielski, C., Baudino, J.-L., Lagage, P.-O., Boccaletti, A., Gastaud, R., Coulais, A., & Bézard, B. 2018, *AJ*, *156*(6), 276.

Davies, R., & Kasper, M. 2012, *ARA&A*, *50*, 305.

Delacroix, C., Absil, O., Forsberg, P., et al. 2013, *A&A*, *553*, A98.

Dorn, M., McMurtry, C., Pipher, J., et al. 2018, in: *Proc. SPIE*, Vol. *10709*, 1070907. https://www.spiedigitallibrary.org/conference-proceedings-of-spie/10709/2313521/A-monolithic-2k-x-2k-LWIR-HgCdTe-detector-array-for/10.1117/12.2313521.short

Ertel, S., Defrère, D., Hinz, P., et al. 2018, *AJ*, *155*(5), 194.

Gardner, J. P., Mather, J. C., Clampin, M., et al. 2006, *Space Sci. Rev.*, *123*(4), 485.

Hinz, P. M., Bouchez, A., Johns, M., Shectman, S., Hart, M., McLeod, B., & McGregor, P. 2010, in: *Proc. SPIE*, Vol. *7736*, 77360C. https://www.spiedigitallibrary.org/conference-proceedings-of-spie/7736/1/The-GMT-adaptive-optics-system/10.1117/12.857968.short

Hoffmann, W. F., Fazio, G. G., Shivanandan, K., Hora, J. L., & Deutsch, L. K. 1993, in: *Proc. SPIE*, Vol. *1946*, 449. https://www.spiedigitallibrary.org/conference-proceedings-of-spie/1946/1/MIRAC-a-mid-infrared-array-camera-for-astronomy/10.1117/12.158697.short

Hoffmann, W. F., Hinz, P. M., Defrère, D., et al. 2014, in: *Proc. SPIE*, Vol. *9147*, 91471O. https://www.spiedigitallibrary.org/conference-proceedings-of-spie/9147/1/Operation-and-performance-of-the-mid-infrared-camera-NOMIC-on/10.1117/12.2057252.short

Hoffmann, W. F., Hora, J. L., Fazio, G. G., Deutsch, L. K., & Dayal, A. 1998, in: *Proc. SPIE*, Vol. *3354*, 647. https://www.spiedigitallibrary.org/conference-proceedings-of-spie/3354/1/MIRAC2-a-mid-infrared-array-camera-for-astronomy/10.1117/12.317327.short

Ives, D., Finger, G., Jakob, G., & Beckmann, U. 2014, in: *Proc. SPIE*, Vol. *9154*, 91541J. https://www.spiedigitallibrary.org/conference-proceedings-of-spie/9154/1/AQUARIUS--the-next-generation-mid-IR-detector-for-ground/10.1117/12.2055837.short

Ives, D., Finger, G., Jakob, G., Eschbaumer, S., Mehrgan, L., Meyer, M., & Steigmeier, J. 2012, in: *Proc. SPIE*, Vol. *8453*, 845312. https://www.spiedigitallibrary.org/conference-proceedings-of-spie/8453/1/AQUARIUS--the-next-generation-mid-IR-detector-for-ground/10.1117/12.925844.short

Jerram, P., & Beletic, J. 2019, in: *Proc. SPIE*, Vol. *11180*, 111803D. https://www.spiedigitallibrary.org/conference-proceedings-of-spie/11180/2536040/Teledynes-high-performance-infrared-detectors-for-Space-missions/10.1117/12.2536040.full

Kasper, M., Arsenault, R., Käufl, H. U., et al. 2017, *Messenger*, *169*, 16.

Kasper, M., Arsenault, R., Käufl, U., et al. 2019, *Messenger*, *178*, 5.

Leisenring, J. M., Rieke, M., Misselt, K., & Robberto, M. 2016, in: *Proc. SPIE*, Vol. *9915*, 99152N. https://www.spiedigitallibrary.org/conference-proceedings-of-spie/9915/1/Characterizing-persistence-in-JWST-NIRCam-flight-detectors/10.1117/12.2233917.short

Lord, S. D. 1992, *NASA Tech. Memo.*, *103957*, 2.

Martinka, M., Almeida, L. A., Benson, J. D., & Dinan, J. H. 2001, *J. Electron. Mater.*, *30*(6), 632.

McMurtry, C., Lee, D., Beletic, J., et al. 2013, *Opt. Eng.*, *52*, 091804.

McMurtry, C. W., Cabrera, M. S., Dorn, M. L., Pipher, J. L., & Forrest, W. J. 2016, in: *Proc. SPIE*, Vol. *9915*, 99150E. https://www.spiedigitallibrary.org/conference-proceedings-of-spie/9915/1/13-micron-cutoff-HgCdTe-detector-arrays-for-space-and-ground/10.1117/12.2233616.short

Moore, A. C., Ninkov, Z., & Forrest, W. J. 2004, in: *Proc. SPIE*, Vol. *5167*, 204. https://www.spiedigitallibrary.org/conference-proceedings-of-spie/5167/1/Interpixel-capacitance-in-nondestructive-focal-plane-arrays/10.1117/12.507330.short

Morzinski, K. M., Montoya, M., Fellows, C., et al. 2020, in: *Proc. SPIE*, Vol. *11448*, 114481L. https://www.spiedigitallibrary.org/conference-proceedings-of-spie/5167/1/Interpixel-capacitance-in-nondestructive-focal-plane-arrays/10.1117/12.507330.short

Neugebauer, G., Habing, H. J., van Duinen, R., et al. 1984, *ApJ*, *278*, L1.

Paalvast, S., Huisman, R., Brandl, B., et al. 2014, in: *Proc. SPIE*, Vol. *9151*, 91510D. https://www.spiedigitallibrary.org/conference-proceedings-of-spie/9151/1/Development-and-characterization-of-a-2D-precision-cryogenic-chopper-for/10.1117/12.2054874.short

Pain, B., & Fossum, E. R. 1993, *Root*, 18. Retrieved from https://dataverse.jpl.nasa.gov/dataset.xhtml?persistentId=hdl:2014/35593.

Pathak, P., Petit dit de la Roche, D. J. M., Kasper, M., et al. 2021, *A&A*, *652*, A121.

Plazas, A. A., Shapiro, C., Smith, R., Huff, E., & Rhodes, J. 2018, *PASP*, *130*(988), 065004.

Regan, M. W., & Bergeron, L. E. 2020, January, *J. Astron. Telesc. Instrum. Syst.*, *6*, 016001.

Ren, B. B., Wallack, N. L., Hurt, S. A., et al. 2023, *arXiv e-prints*, arXiv:2301.07714.

Rieke, G. 2002, *Detection of Light*, Cambridge University Press, Cambridge.

Rieke, G. H., Wright, G. S., Böker, T., et al. 2015, *PASP*, *127*(953), 584.

Schlawin, E., Leisenring, J., McElwain, M. W., et al. 2021, *AJ*, *161*(3), 115.

Stapelbroek, M. G., Petroff, M. D., Speer, J. J., & Bharat, R. 1984, *Origin of Excess Low Frequency Noise at Intermediate Infrared Backgrounds in BIB Detectors. Proc.* (IRIS Detector, No. 2). Proceedings IRIS Specialty Group on Infrared Detectors (August 1984, Seattle, WA).

Tam, S., & Hu, C. 1984, *IEEE Trans. Electron Devices*, *31*, 1264.

Tennant, W. E. 2010, *J. Electron. Mater.*, *39*(7), 1030.

Tennant, W. E., Lee, D., Zandian, M., Piquette, E., & Carmody, M. 2008, *J. Electron. Mater.*, *37*(9), 1406.

Viswanath, G., Janson, M., Dahlqvist, C.-H., et al. 2021, *A&A*, *651*, A89.

Wagner, K., Boehle, A., Pathak, P., et al. 2021, *Nat. Commun.*, *12*, 922.

Wright, G. S., Wright, D., Goodson, G. B., et al. 2015, *PASP*, *127*(953), 595.

AUTHOR BIOGRAPHY

Jarron Leisenring is an Assistant Research Professor at the University of Arizona with a PhD in Astronomy from the Univeristy of Virginia received in 2011. In 2013, he joined Steward Observatory at the University of Arizona as part of the JWST NIRCam instrument team. His research interests include infrared detector technology development, instrumentation for high contrast imaging, and the detection and characterization of exoplanets.

How to cite this article: Leisenring, J. M., Atkinson, D., Bowens, R., et al. 2023, *Astron.Nachr./AN*, *344*, e230103. https://doi.org/10.1002/asna.20230103